Journal of Basic & Applied Sciences, 2025, *21*, 128-135

Published by SET Publisher

Journal of Basic & Applied Sciences

ISSN (online): 1927-5129

Numerical Simulation of a Turboprop Engine Inlet with a Bypass Channel

Zhanwang Liu[1], Zhenlong Wu[1,*] and Yakui Liu[2]

[1]*College of Energy and Power Engineering, Nanjing University of Aeronautics and Astronautics, Nanjing 211106, Jiangsu Province, People's Republic of China*

[2]*State Key Laboratory of Aerodynamics, Mianyang, 621000, Sichuan Province, China*

Article Info:

Keywords:
Computational Fluid Dynamics,
Turboprop engine inlet,
Sand separation,
Bypass channel,
Parametric influence.

Timeline:
Received: April 29, 2025
Accepted: May 22, 2025
Published: June 24, 2025

Citation: Liu Z, Wu Z, Liu Y. Numerical simulation of a turboprop engine inlet with a bypass channel. J Basic Appl Sci 2025; 21: 128-135.

DOI: https://doi.org/10.29169/1927-5129.2025.21.13

*Corresponding Author
E-mail: zhenlongwu@nuaa.edu.cn

Abstract:

Turboprop aircraft may face a variety of harsh flight environments during flight, and various foreign objects may be sucked into the engine, among which the inhalation of sand can lead to erosion of the blades of the compressor. Such ingestion often results in compressor blade erosion, which can lead to engine surge and power loss. Therefore, this study explores the aerodynamic and sand separation characteristics of the inlet channel with a bypass channel through numerical simulation methods. ANSYS Fluent software is used to simulate the six-bladed propeller rotation based on the slip-grid technique by combining the unsteady Reynolds-averaged Navier-Stokes equations (URANS) and shear stress transport (SST) turbulence model. A Lagrangian discrete phase model (DPM) is applied to track the motion of standard coarse sand. The focus is on analyzing the mechanism of different propeller speeds and scavenge ratio (SCR) on the separation efficiency (η).

1. INTRODUCTION

Turboprop engines are vital for regional airliners and military transport, offering high fuel efficiency, short takeoff and landing (STOL) capability, cost-effectiveness, and robust adaptability [1]. However, turboprop engines operate in diverse and complex flight environments, including sandstorm conditions that pose significant sand ingestion risks. Sand ingestion leads to progressive erosion of the compressor blades, which can ultimately cause engine surge and power loss [2]. Therefore, it is crucial for turboprop engine inlets to possess excellent foreign object rejection capability. In order to prevent foreign objects from being sucked into the inlet and entering the engine, researchers have developed a turboprop engine inlet with a bypass channel [3]. Compared to a conventional inlet, it features an additional channel dedicated to the discharge of foreign matter that prevents sand and other debris from entering the engine. Current research [4-7] primarily focuses on inertial separator characteristics and foreign object ingestion trajectories, whereas studies on separation characteristics within turboprop inlet bypass channels remain scarce. Specifically, research on sand separation performance in turboprop inlets with bypass channels is notably scarce. Therefore, this study employs numerical simulations to analyze the aerodynamic and sand separation performance of a bypass-equipped turboprop engine, aiming to provide theoretical and data-driven insights for optimizing foreign object debris (FOD) rejection in turboprop inlet bypass channel designs.

2. NUMERICAL METHOD

2.1. CFD-DPM Coupling Scheme

The unsteady Reynolds-averaged Navier-Stokes (RANS) equations were solved using the pressure-based solver in ANSYS Fluent. The shear-stress transport (SST) k-ω turbulence model was employed for closure. Spatial discretization was performed as follows:

(1) Gradients were computed using the least-squares cell-based method.

(2) Pressure interpolation was treated with a second-order scheme.

(3) All other variables were discretized using a second-order upwind scheme.

A first-order implicit formulation was adopted for temporal discretization. The dynamic behavior of sand particles was simulated using a discrete phase model (DPM) with Lagrangian particle tracking. The numerical simulation employed a sliding mesh approach, where surfaces in the rotating domain move synchronously with the propeller rotational speed. Data transfer between the propeller and flow field was achieved through the interface separating the stationary and rotating domains. The particle size distribution of sand was calculated according to the Rosin-Rammler size distribution. The distribution function was based on the assumption that an exponential relationship exists between the particle diameter d and the mass fraction of particles with diameter greater than d is Y_d. The Y_d was obtained by equation applying:

$$Y_d = e^{-(d/\bar{d})^n} \tag{1}$$

Where $\bar{d}$ in equation as the mean diameter and to n as the spread parameter. According to GJB 242A-2018 General specification for aerospace turboprop and turboshaft engines it is possible to obtain an average particle size of 295.56 μm for standard coarse sand with a spread parameter. of 1.68.

2.2. Physical Parameter Definition

For turboprop engine inlet, the main parameters to evaluate its performance are total pressure recovery coefficient (σ) and distortion index, commonly used distortion parameters are total pressure distortion index DC60, DC90, etc. In this paper, DC60 is selected as the distortion parameter for this study, which is defined as follows:

$$DC60 = \frac{p_{AIP} - p_{min60^\circ}}{q_{av}} \tag{2}$$

where p_{min60° is the minimum total pressure in any sector region with the phase angle of 60° and q_{av} is the average dynamic pressure at AIP.

$$\sigma = \frac{p_{AIP}}{p_0} \tag{3}$$

where p_{AIP} is the area-weighted average total pressure at the AIP and p_0 is the freestream total pressure. The equation for the scavenge ratio (SCR) is as follows:

$$SCR = \frac{m_s}{m_c} \tag{4}$$

where m_s is the mass flow rate [kg/s] in the bypass channel, m_c is the mass flow rate in the core channel. The calculation formula for the sand separation on efficiency of the inlet η is as follows:

$$\eta = \frac{M_b}{M_b + M_c} \tag{5}$$

where M_b is the mass of sand entering the bypass channel, M_c is the mass of sand entering the core channel.

2.3. Mesh Convergence Analysis and Temporal Independence Verification

The entire computational domain is using an unstructured mesh, and the boundary conditions for the pressure far field and the pressure outlet are set up, and the nacelle wall and the inlet duct wall are used as no-slip walls. The model is a six-bladed propeller. This mesh was drawn by ICEM software as shown in Figure **1**. To verify grid independence, three distinct mesh systems were employed: coarse (6.5 million), medium (10.8 million), and dense (16.4 million) grids. Figure **2** presents the critical AIP (Aerodynamic Interface Plane) mesh configurations under different grid resolutions. As evidenced in Table **1**, the variations between medium and dense grids are negligible, indicating that grid independence has been achieved at the medium resolution of 10.8 million elements. Consequently, the medium grid system was selected for all subsequent computational analyses in this study. There was also a set of mesh without propellers with 4~5 million. Similarly, to verify temporal independence, four distinct time steps corresponding to 5°, 2°, 1°, and 0.5° were systematically evaluated. As shown in Figure **3**, the numerical solutions exhibit negligible variations between the 1° and 0.5° cases, confirming time-step

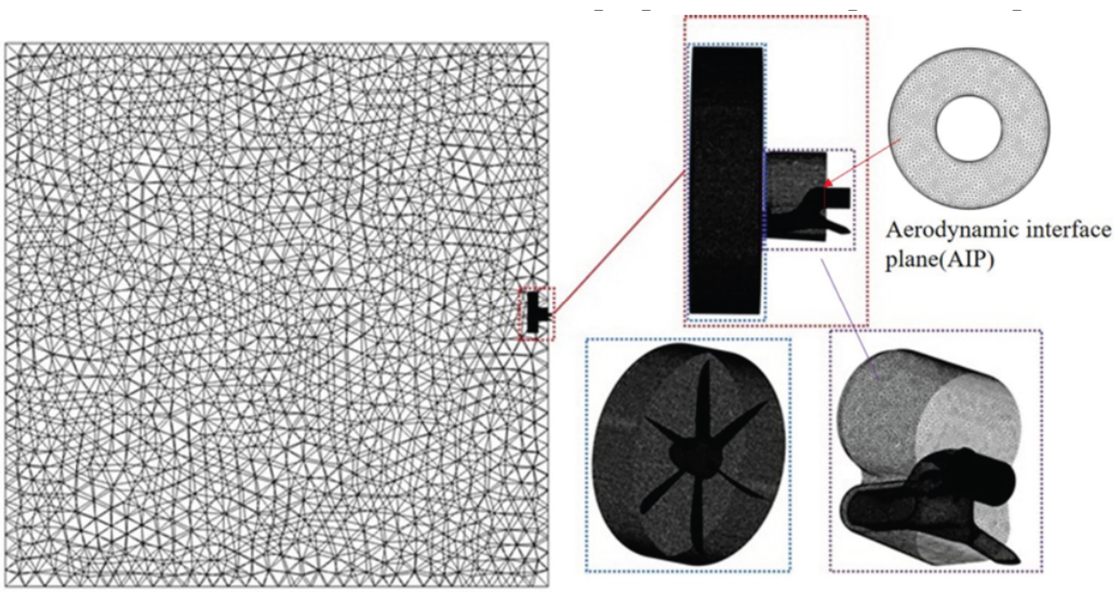

Figure 1: The mesh generated by ICEM.

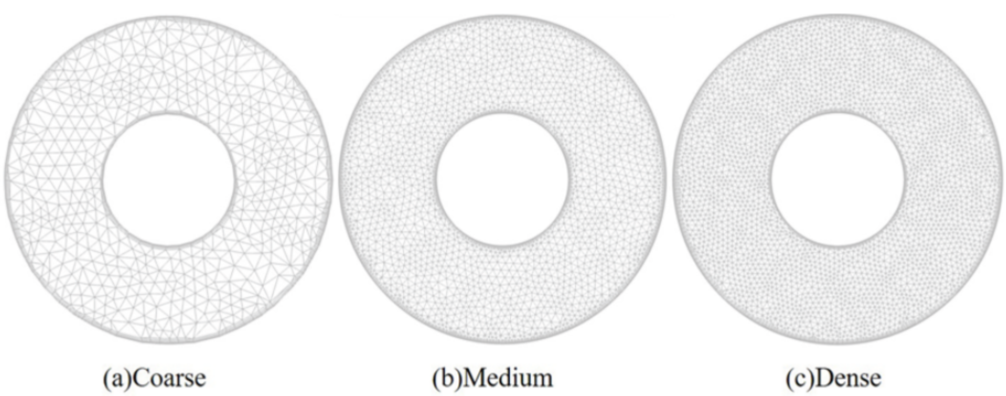

Figure 2: AIP surfaces with varying grid densities.

independence at 1° resolution. Therefore, the time step size was set to be equivalent to 1° of propeller rotation per time step.

Table 1: Aerodynamic Performance Characteristics at the AIP Across Varying Grid Densities

	Coarse	Medium	Dense
σ	1.0038	1.0061	1.0059
DC60	0.2545	0.2483	0.2487

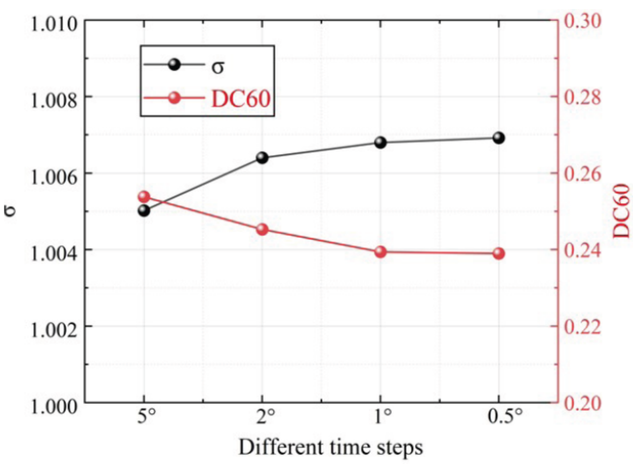

Figure 3: Temporal independence verification.

2.4. Validated Numerical Methodology

As demonstrated in Figure **4**, the numerical results show good agreement with experimental data, with a maximum deviation of less than 2% in key aerodynamic parameters. The simulation results were obtained using a quasi-steady approach that integrates sliding mesh technology with steady-state particle injection. Data sampling was performed at 5-degree intervals, followed by multi-condition averaging to ensure statistical convergence.

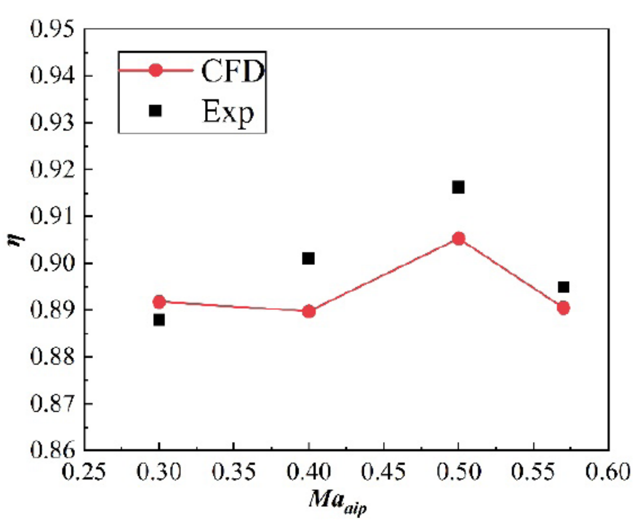

Figure 4: Comparison between simulation and experimental results.

3. RESULTS AND DISCUSSION

3.1. Aerodynamic Characteristics of a Turboprop Inlet under the Influence of Propeller Airflow

Figure **5** shows the AIP Mach number and total pressure coefficient cloud without propeller, and it can be seen that both the AIP surface Mach number and total pressure coefficient contour plot are approximately symmetrically distributed without propeller interference. Its total pressure recovery coefficient at the AIP surface is 0.9872 and its distortion DC60 is 0.0619. This indicates that the flow is relatively uniform and balanced when the propeller is not working. The low total pressure recovery coefficient regions are mainly distributed on the left and right sides of the upper section near the inner wall, the upper sector and the shielded area downstream of the guide vane, which may have reduced pressure due to separation of the flow or other factors.

For the simulation with the influence of a propeller, the data is saved at 60° phase angle intervals since the propeller is a six-bladed propeller. The average value of the influence of the propeller on the airflow can be calculated. Figure **6** shows the Mach number and σ distribution of the AIP for different phase angles. The airflow is twisted in the direction of rotation in the presence of propeller interference. The regions with low total pressure recovery coefficients are mainly distributed in the left and right sides of the upper half of the sector, the left side of the lower half of the sector, and the shielding region downstream of the guide vanes. The low Mach number region is mainly distributed in the upper left of the sector with vortex generation. The Mach number and total pressure recovery coefficient cloud plots do not differ much at each 60° phase turn, and the streamline plots show that there are only localized differences, which implies that the performance of the propeller is relatively stable at different phase angles. The mean Mach number, total pressure recovery coefficient σ, and DC60 of the inlet AIP surface at different phase angles are shown in Table **2**. Observing the distortion index DC60, it is found to be on the high side, which is due to the fact that the airflow generated by the rotating propeller will form a slipstream, which may disturb the airflow in the inlet and lead to uneven airflow distribution inside the inlet, thus increasing the distortion index.

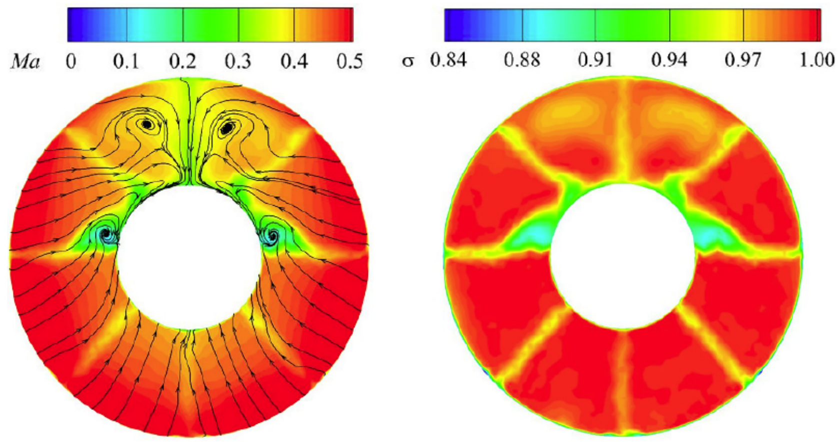

Figure 5: Mach number and total pressure recovery coefficient distributions for the main channel AIP surface without propeller.

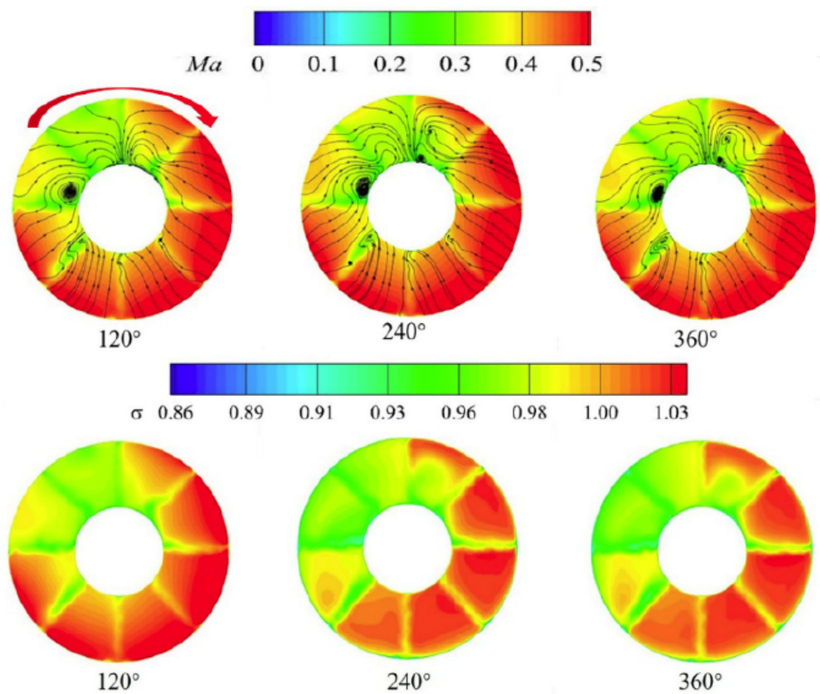

Figure 6: The distribution of Mach number and total pressure recovery coefficient at AIP under different phase angles.

Table 2: The Mean Mach Number, σ and DC60 for Different Phase Angles

Phase angle	60°	120°	180°	240°	300°	360°
Maip	0.42	0.4203	0.4215	0.4209	0.4215	0.4216
σ	0.9942	0.9952	0.9975	0.9974	0.9970	0.9961
DC60	0.2925	0.2856	0.2812	0.2965	0.2930	0.2874

3.2. Standard Coarse sand Separation Characteristics for Turboprop Inlets

The sand injection simulation was carried out every sixty degrees of rotation of the propeller, and the separation efficiencies obtained are shown in Table **3**. The average separation efficiency of the standard coarse sand obtained by rotating the first rotation is 0.5840, and the average separation efficiency obtained by rotating the second rotation is 0.5891. Both errors are not large, which indicates that the simulation method has a certain degree of accuracy. The

Table 3: Separation Efficiency of the Inlet

Phase angle	60°	120°	180°	240°	300°	360°	Average separation efficiency
Standard coarse sand(a)	0.5985	0.5969	0.5712	0.5971	0.5814	0.5593	0.5840
Standard coarse sand(b)	0.5853	0.6087	0.5991	0.5772	0.5799	0.5843	0.5891

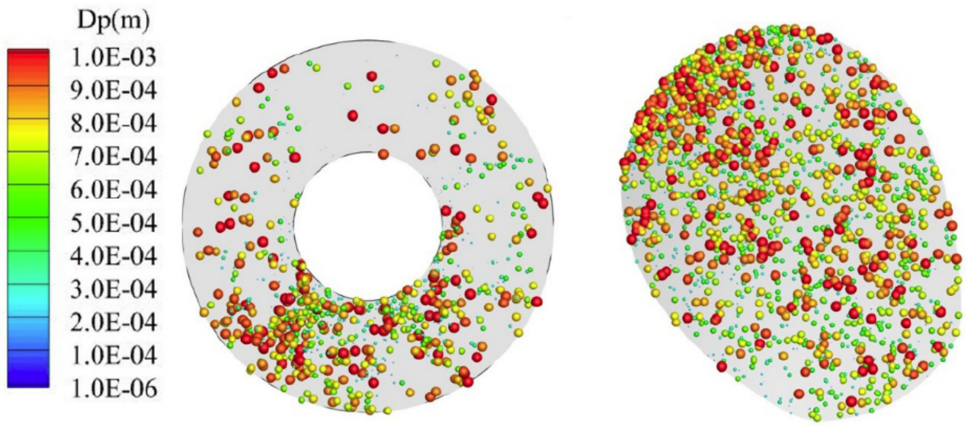

Figure 7: The distribution of sand particles in the core and bypass channels.

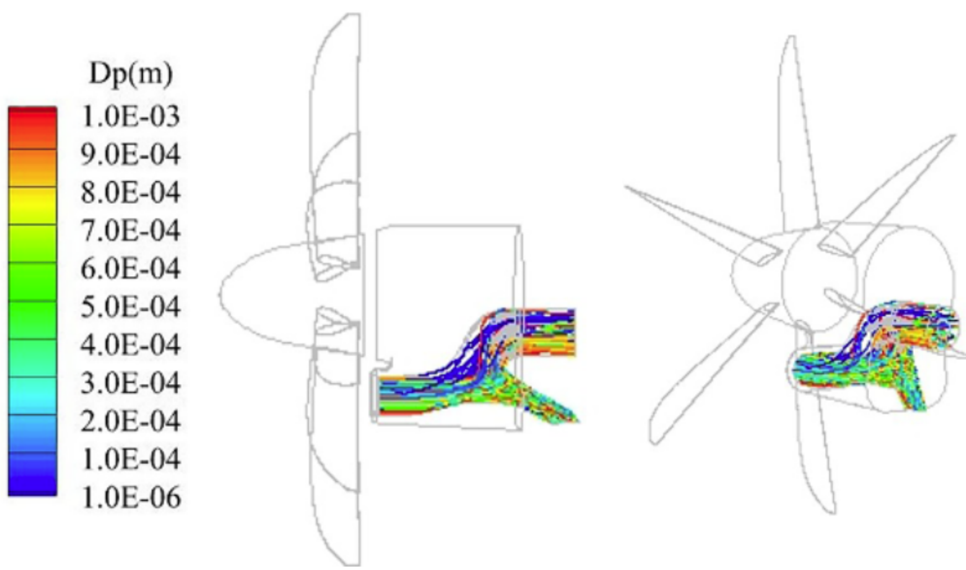

Figure 8: Three-dimensional particle trajectory diagrams from different perspectives.

distribution of sand particles in the core and bypass channels is shown in Figure **7**. The number of particles in the core and bypass channels was reduced for ease of observation. With the core channel on the left and the bypass channel on the right, it can be seen that the vast majority of the sand is distributed in the bypass channel. It is also possible to observe that most of the particles are located below, due to the influence of gravity. Figure **8** shows the three-dimensional particle trajectories from different angles. The visualization employs a 500:1 particle count reduction to enhance clarity while maintaining flow field representativeness. It is also possible to see that most of the particles are discharged from the bypass channel.

Figure **9** illustrates the variation of the separation efficiency of the sand as a function of the scavenge ratio. It can be seen that the separation efficiency of the coarse sand increases with the gradual increase of the scavenge ratio. This phenomenon occurs because increasing the bypass channel flow rate reduces the core channel airflow velocity. The consequent decrease in aerodynamic drag forces diminishes the inertial effects on coarse sand particles, enhancing their capture efficiency. However, in order to increase the scavenge ratio, the outlet back pressure needs to be continuously reduced, so the scavenge ratio cannot be increased indefinitely. Therefore, increasing the scavenge ratio only increases the sand separation efficiency within a certain range.

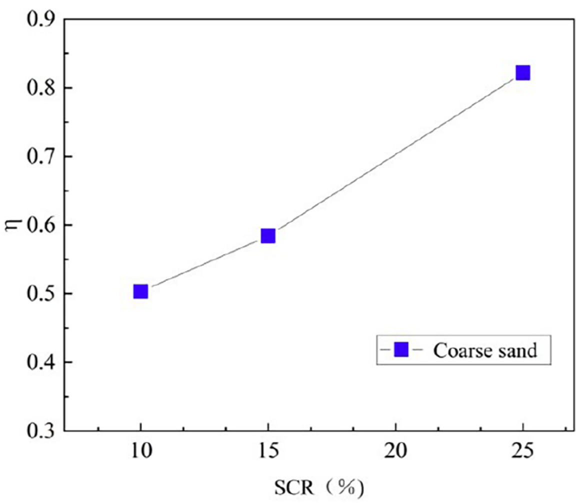

Figure 9: The separation efficiency of sand varies with the SCR.

From Figure **10**, it can be seen that the separation efficiency of coarse sand decreases gradually as the propeller speed increases. Although the inlet flow rate and airflow velocity (U) increase with higher propeller speed and the Stokes number is proportional to U, the separation efficiency does not increase monotonically. The reasons are that the acceleration of the airflow makes more small particles enter the main channel with the airflow. Higher airflow velocities shorten the residence time of the particles in the separation channel, which means that coarse sand may not have enough time to settle before it is carried away.

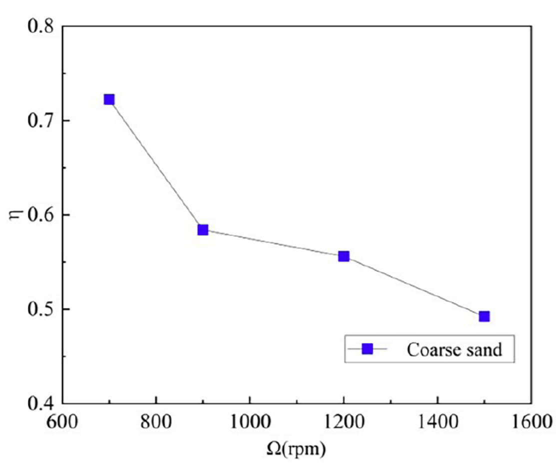

Figure 10: The separation efficiency of sand varies with the rotational speed of the propeller.

The variation law of the separation efficiency of sand at different angles of attack and different exit Mach numbers was also investigated. With the change of angle of attack and outlet Mach number of the inlet channel, the separation efficiency of coarse sand basically remains unchanged.

4. CONCLUSIONS

In order to investigate the sand rejection characteristics of a turboprop engine inlet with a bypass channel, CFD numerical simulation is used in this study. The sand separation efficiency under different parameters is analyzed, thus revealing the coupling mechanism between particle behavior and airflow dynamics. The main conclusions are as follows:

(1) The presence of propeller work can increase the total pressure recovery coefficient, but it also leads to an increase in the total pressure distortion DC60.

(2) Increasing the scavenge ratio (SCR) improves separation efficiency but has practical limitations.

(3) Higher propeller rotational speeds detrimentally impact sand separation efficiency.

(4) The study provides valuable CFD methodology and performance data for optimizing sand separation in turboprop engine inlets with bypass channel.

ACKNOWLEDGEMENTS

This research was partially supported by the open subject of State Key Laboratory of Aerodynamics of China under grant RAL202402-7 and the National Science and Technology Major Project under grant HT-J2019-V-0004-0095.

CONFLICT OF INTEREST

The authors declare that they have no known competing financial interests or personal relationships that could have appeared to influence the work reported in this paper.

AUTHORS CONTRIBUTION

Zhanwang Liu: Writing of the original draft, software, Methodology; **Zhenlong Wu**: Review and editing; **Yakui Liu:** Formal analysis and data curation.

REFERENCES

[1] Zheng G, Tan H, Wu Z, Zhang F, Zhang Y, Luo G. Aerodynamics and bird ingestion characteristics of a bulge-adjustable turboprop engine inlet. Aerospace Science and Technology 2024; 144: 108777.
https://doi.org/10.1016/j.ast.2023.108777

[2] Liu R, Pan Y, Chen A, Bin G, Li H. Study on the influence of surface roughness on the erosion characteristics of compressor blades. Powder Technology 2023; 430: 119037.
https://doi.org/10.1016/j.powtec.2023.119037

[3] Zheng G, Wu Z, Tan H, Zhang Y, Wang K. Design and examination of a turboprop inlet with scavenge duct. Chinese Journal of Aeronautics 2023; 36(8): 32-42.
https://doi.org/10.1016/j.cja.2023.04.014

[4] Ghenaiet A, Tan SC, editors. Numerical Study of an Inlet Particle Separator. ASME Turbo Expo 2004: Power for Land, Sea, and Air; 2004.
https://doi.org/10.1115/GT2004-54168

[5] Taslim ME, Spring S. A Numerical Study of Sand Particle Distribution, Density, and Shape Effects on the Scavenge Efficiency of Engine Inlet Particle Separator Systems. Journal of the American Helicopter Society 2010; 55(2): 022006.
https://doi.org/10.4050/JAHS.55.022006

[6] Barone DL, Loth E, Snyder PH. Efficiency of an Inertial Particle Separator. Journal of Propulsion and Power 2015; 31: 997-1002.
https://doi.org/10.2514/1.B35276

[7] Du Z, Ma Y, Xu Q, Wu F. Sand Discharge Simulation and Flow Path Optimization of a Particle Separator 2023; 25(1): 147.
https://doi.org/10.3390/e25010147